Drops and bubbles in wedges

Etienne Reyssat

Drops and bubbles in wedges

Etienne Reyssat[1]†

[1]PMMH, CNRS UMR 7636 - ESPCI - UPMC Université Paris 6 - UPD Université Paris 7, 10 rue Vauquelin, 75005 Paris, France, EU

(Received ?; revised ?; accepted ?. - To be entered by editorial office)

We investigate experimentally the spontaneous motion of drops and bubbles confined between two plates forming a narrow wedge. Such discoidal objects migrate under the gradient in interfacial energy induced by the non-homogeneous confinement. The resulting capillary driving force is balanced by viscous resistance. The viscous friction on a drop bridging parallel plates is estimated by measuring its sliding velocity under gravity. The viscous forces are the sum of two contributions, from the bulk of the liquid and from contact lines, the relative strength of which depends on the drop size and velocity and the physical properties of the liquid. The balance of capillarity and viscosity quantitatively explains the dynamics of spontaneous migration of a drop in a wedge. Close the tip of the wedge, bulk dissipation dominates and the migrating velocity of drops is constant and independent of drop volume. The distance between the drop and the tip of the wedge is thus linear with time t: $x(t) \sim t_0 - t$, where t_0 is the time at which the drop reaches the tip of the wedge. Far away from the apex, contact lines dominate the friction, the motion is accelerated toward the tip of the wedge and velocities are higher for larger drops. In this regime, it is shown that $x(t) \sim (t_0 - t)^{4/13}$. The position and time of the crossover between the two dissipation regimes are used to write a dimensionless equation of motion. Plotted in rescaled variables, all experimental trajectories collapse to the prediction of our model. In contrast to drops, gas bubbles in a liquid-filled wedge behave as non-wetting objects. They thus escape the confinement of the wedge to reduce their surface area. The physical mechanisms involved are similar for drops and bubbles, so that the forces acting have the same mathematical structures in both cases, except for the sign of the capillary driving force and a numerical factor. We thus predict and show experimentally that the trajectories of drops and bubbles obey the same equation of motion,except for a change in the sign of $t_0 - t$.

Key words:

---

1. Introduction

When deposited at the boundary between a wetting and a non-wetting substrate, a liquid drop shifts towards the region of higher wettability (Weislogel 1997). More generally, when confronted with a gradient in the surface energy of the substrate, drops move towards the most wettable region. Genzer & Bhat (2008) discuss the nature, strength, directionality, scale, dynamical properties and functionalities of such surface-gradient-induced motions. The wettability gradient may have a chemical origin, if the surface coating is not uniform. Greenspan (1978) first proposed a model to explain the motion of a droplet on such a chemically non-uniform coating and related this phenomenon to the

† Email address for correspondence: etienne.reyssat@espci.fr

experimental observation of cells migrating on heterogeneous surfaces. Inhomogeneities in the spreading coefficient due to chemistry or temperature gradients have been shown to set droplets in motion (Brochard 1989). Without the Marangoni effect, using surfaces with a hydrophobicity gradient, Chaudhury & Whitesides (1992) induced the motion of water droplets over centimetric lengths. Contact angle hysteresis may prevent migration from occuring and pin droplets on local minima of the interfacial energy. In this case, it has been shown that mechanical shaking can reduce or suppress the effect of hysteresis and set the drop into motion (Daniel *et al.* 2004). Such systems, however, usually enable motion over relatively short distances as the range of available surface energies is limited. Drops containing surface-active molecules have been shown to generate a wettability asymmetry themselves and maintain self-propulsion over long distances (Domingues dos Santos & Ondarçuhu 1995). It is also possible to induce drop migration without using chemistry. Gradients in the mechanical or geometrical properties of the environment induce long-range motion of drops. It has recently been shown (Style *et al.* 2013) that drops move toward soft regions of substrates with stiffness gradients, a process reminiscent of cell durotaxis (Lo *et al.* 2000). Superhydrophobic surfaces can be manufactured with a texture gradient. A drop sitting on such an inhomogeneous rough texture was shown to drift when activated by mechanical shaking of the surface (Reyssat *et al.* 2009). Nanometric anisotropic textures also rectify the motion of vibrated drops through a ratchet-like mechanism (Malvadkar *et al.* 2010). Bouasse (1924) suggested that a drop placed inside a tapered capillary tube should move towards the tip of the cone. Renvoisé *et al.* (2009) recently revisited this experiment and addressed the problem of the equilibrium of a liquid index submitted to its weight in a tapered tube. In a symmetric setting, Lorenceau & Quéré (2004) demonstrated that a drop of oil on a conical wire escapes the tip of the cone and spreads onto the relatively thick regions. On Earth, capillary driven flows commonly occur in small-size systems, where volumic forces are dominated by interfacial effects. The migration of drops in confinement gradients has recently been proposed as a useful tool for droplet manipulation in microfluidics (Dangla *et al.* 2013; Selva *et al.* 2011; Metz *et al.* 2009). In microgravity, confinement inhomogeneities become relevant tools to manipulate fluids at larger length scales (Weislogel & Lichter 1996; Weislogel *et al.* 2011). The motion of drops in geometric gradients is also of relevance to the biological world. Spindle-knot structures along silk threads tend to attract dew drops that collect on spider webs (Zheng *et al.* 2010). The drinking mechanism of the phalarope shorebird also relies on the capillary motion of water drops under the tweezering opening and closing motion of its beak (Prakash *et al.* 2008).

Three centuries ago, Hauksbee (1710) reported that a drop of oil of orange placed between two glass plates forming a sharp wedge migrates towards the most confined region. In the present paper, we explain the dynamics of drops and bubbles confined in wedges by a balance of capillary and viscous forces. We first calibrate the friction forces by measuring the migration velocities of oil drops sliding under gravity between parallel plates. We then experimentally demonstrate the existence of two asymptotic regimes for a drop drifting inside a sharp wedge. Distinct limits correspond to different dissipation mechanisms resisting the capillary driving force. By writing the equation of motion in a dimensionless form, one is able to describe all experimental drop trajectories. The same phenomenology is shown to apply to air bubbles escaping confinement in immersed wedges. Finally, we extend our results to the migration of drops and bubbles in wedges with power-law shapes.

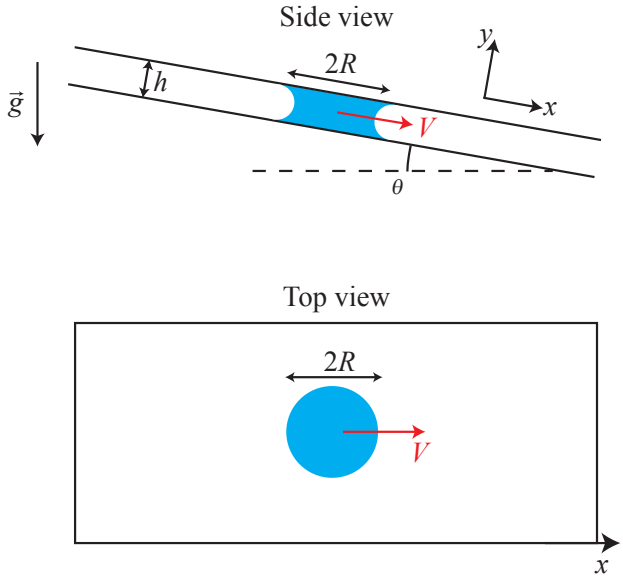

FIGURE 1. A circular liquid drop of radius R is bridging to parallel glass plates separated by a gap of thickness h. As the cell is tilted with an angle θ, the drop moves under gravity at constant velocity V.

2. Drops sliding down an inclined Hele-Shaw cell

2.1. *Experimental set-up*

We first perform experiments in a classical Hele-Shaw geometry to calibrate the friction mechanisms. Two parallel glass plates are separated by glass or plastic spacers along their boundaries to create a uniform thin gap. The gap thickness h ranges from 150 to 1100 μm. Using a syringe needle, we insert a drop of silicone oil that forms a capillary bridge between the walls of the Hele-Shaw cell (see figure 1). The radius R of these discoidal drops is millimetric to centimetric and their volume Ω ranges from 14 to 1500 μL. The Hele-Shaw cell is then tilted with respect to the horizontal by an angle θ of order $1 \pm 0.2°$, measured with a digital inclinometer. The drop then slides at a constant velocity V under its own weight. A uniform LED backlighting panel is placed below the Hele-Shaw cell and drops are imaged from above using a digital camera. We use silicone oils of viscosity η ranging from 4.1 to 44 mPa.s and surface tension $\gamma \simeq 20$ mN/m. The measured drop velocity is between 0.1 and 5 mm.s^{-1} for oil of viscosity $\eta = 4.1$ mPa.s.

2.2. *Model*

The driving force for the sliding motion is the component W of the weight of the drop along the maximum slope direction, $W = \pi R^2 h \rho g \sin\theta$. Viscosity resists migration and occurs through two distinct mechanisms: part of the dissipation occurs in the bulk of the drop and an additional contribution comes from the contact lines along the drop boundaries. This configuration is reminiscent of experiments on "falling slugs" in capillary tubes, where the authors show that dissipation occurs in the bulk but also at contact lines (Bico & Quéré 2001). We now detail both friction mechanisms.

2.2.1. *Bulk dissipation*

To provide a prediction of the drag contribution of the bulk of the liquid, we first image the flow pattern using small tracing particles. We use 50 μm diameter polyamid beads

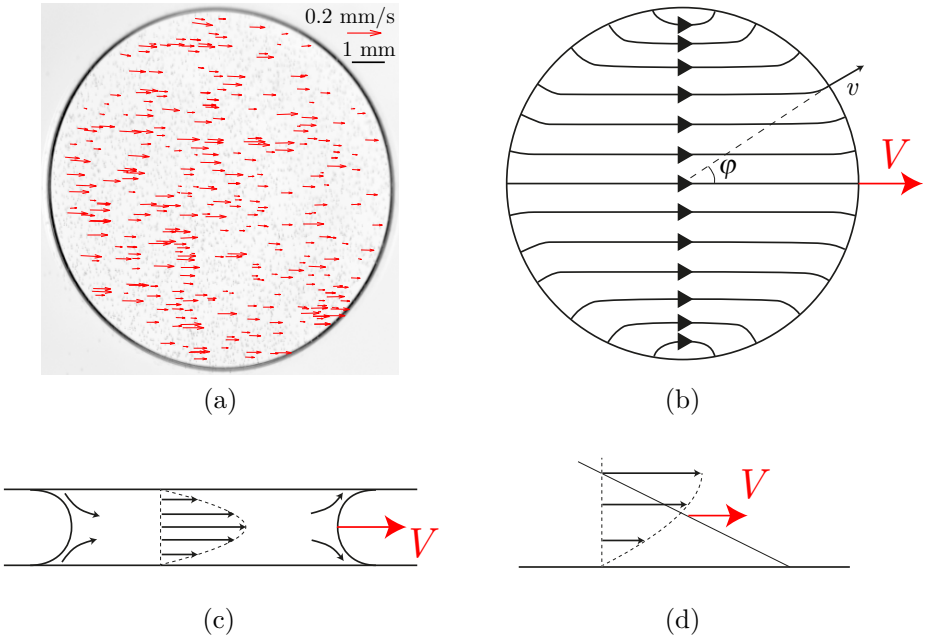

FIGURE 2. Stream lines in a drop sliding between two parallel plates. (a) Velocities of a number of 50 μm diameter polyamide particles suspended in a drop of silicone oil in a 1 mm thick Hele-Shaw cell. The oil viscosity is $\eta = 44$ mPa.s and the drop radius is $R = 5.3$ mm. All particles are observed to move to the right of the picture, as the drop itself, revealing a simple flow pattern with straight streamlines. The velocity field is depth-dependent: slow velocities correspond to particles close to the walls, while fast tracers are at the center of the cell. The quickest particles move at 0.128 mm/s , while the drop sliding velocity is 0.085 mm/s. (b) Top view. Sketch of theoretical streamlines. In most of the fluid, the flow is directed along the migration direction of the drop. In the vicinity of contact lines, stream lines bend and are perpendicular to the drop boundary. The local advancing velocity of the contact line is $v = V \cos\varphi$. (c) Cross section of a central cut of the drop along the direction of motion. In the bulk of the drop, the velocity follows a parabolic Poiseuille profile. The flow deviates from this profile only close to the drop boundary. (d) In the vicinity of contact lines, the structure of the advancing front is close to a wedge. The flow is again of Poiseuille type, with no-slip at the solid-liquid interface and no-stress at the upper liquid/gaz interface. The average velocity along the motion direction is the migration velocity V of the drop.

suspended in a drop of silicone oil bridging the parallel plates of a 1 mm thick Hele-Shaw cell. The device is tilted by an angle of order 1° with respect to the horizontal, so that the drop slides under its own weight. The drop is then imaged from above, and we track the positions of the particles in time to extract their velocities and the streamlines. In figure 2a, we show the velocities of beads placed in a drop of silicone oil with viscosity $\eta = 44$ mPa.s. All particles are seen to move parallel to the global drop motion, with different velocities. Fluid moves along parallel straight lines from the rear to the front of the drop. The velocity of the quickest tracing particles is 1.5 times the velocity of the drop boundary. The flow in the drop is thus mainly a Poiseuille flow in the direction Ox of motion of the drop. The x component v_x of the velocity field depends on the y coordinate and is expressed as

$$v_x(y) = \frac{3}{2} V \left(1 - \left(\frac{2y}{h}\right)^2\right) \tag{2.1}$$

where V is the sliding velocity of the drop. The resulting viscous stress at the plates is thus

$$\sigma_\eta = \eta \left| \frac{\partial v_x}{\partial y} \left(\pm \frac{h}{2} \right) \right| = 6\eta \frac{V}{h} \tag{2.2}$$

and the total force $F_{\eta_{bulk}}$ of the plates on the drop is the viscous stress integrated over the top and bottom solid-liquid contact areas,

$$F_{\eta_{bulk}} = 2\pi R^2 \sigma_\eta = 12\eta \frac{V}{h} \pi R^2 \tag{2.3}$$

or

$$F_{\eta_{bulk}} = 12 \frac{\pi R^2}{h} \gamma Ca \tag{2.4}$$

where γ is the surface tension of the liquid and $Ca = \eta V/\gamma$ is the capillary number.

2.2.2. *Contact line drag*

The singular region of contact lines around the drop also contributes to viscous dissipation. The front boundary of the drop advances on the dry solid. The receding meniscus at the rear of the drop deposits a thin liquid film on the plates. Both of these interfacial mechanisms give rise to a viscous drag per unit length of a boundary moving perpendicular to itself that essentially scales as $\gamma Ca^{2/3}$ (de Gennes *et al.* 2004). In the present experiment of a drop bridging the plates of a Hele-Shaw cell, imaging of the flow close to the drop boundaries was not possible as the small solid tracers are hidden by reflections on the curved meniscus at the periphery of the drop. However, in the closely related situation of a drop sliding down a single inclined plate, Rio *et al.* (2005) show experimentally that the flow velocity is normal to contact lines in the vicinity of the drop boundary. We assume that this remains true for the present experiment, as sketched in figure 2b. In a stationary regime, the boundary of the drop does not deform, so that one can define the velocity v of the moving contact line locally along the boundary. Since the drop contour does not deform during the experiment, the local velocity is $v = V \cos\varphi$ where φ is the angle between the drop velocity and the local moving direction of the boundary, as defined in figure 2b. Similarly, we define the local capillary number $ca = Ca \cos\varphi$. Any element of length $\mathrm{d}\ell$ of the contact line thus experiences a force normal to itself and proportional to $\gamma ca^{2/3}\mathrm{d}\ell$. Following the work of Eck & Siekmann (1978) on the motion of bubbles in Hele-Shaw cells, one can project the force contribution from all elements of the contact line and sum them to yield a global force proportional to $\gamma Ca^{2/3}$. The drop has two circular contact lines of length $2\pi R$ each, so that the associated force is

$$F_{\eta_{line}} = 4\pi R \beta \gamma Ca^{2/3} \tag{2.5}$$

where β is of the order of unity and is linked to the details of the contact lines and to the geometry.

We now discuss the value of β. At the rear of the drop, the meniscus is receding and deposits a film of oil, the thickness of which was established by Landau & Levich (1942). For a receding meniscus, the viscous stress applied by the solid on the moving meniscus can be computed exactly. Cantat (2013) gives the force f_r per unit length on a receding meniscus with a local capillary number ca,

$$f_r = 3.84\gamma ca^{2/3} = 3.84\gamma \left(Ca \cos\varphi\right)^{2/3} \tag{2.6}$$

The contribution of force per unit length projected along the direction of motion of the drop is then

$$f_{r/\!/} = 3.84\gamma Ca^{2/3} \left(\cos\varphi\right)^{5/3} \tag{2.7}$$

We integrate this force along the rear boundaries of the drop to obtain the corresponding viscous force (Eck & Siekmann 1978),

$$F_r = \int f_{r/\!/} \mathrm{d}\ell = 4 \int_{\varphi=0}^{\pi/2} 3.84 \gamma R C a^{2/3} \cos\varphi^{5/3} \mathrm{d}\varphi \tag{2.8}$$

or

$$F_r \simeq 12.9 \gamma R C a^{2/3} \tag{2.9}$$

At the front of the drop, the meniscus advances on the dry solid. The force exerted on an advancing interface has been the subject of numerous research papers in the past. The apparent paradox of stress divergence or no-slip condition violation close to a three-phase advancing contact line (Huh & Scriven 1971; Tanner 1979) has been dealt with by several models attempting to regularize the singularity (Eggers & Stone 2004; Bonn *et al.* 2009). The physical mechanisms involved include slip at the solid-liquid interface (Huh & Scriven 1971; Thompson & Troian 1997), the shear-thinning properties of the fluid (Gorodtsov 1989), precursor films (de Gennes 1985), diffuse interfaces (Seppecher 1996; Jacqmin 2000), normal stresses (Boudaoud 2007), fluid evaporation and condensation (Wayner 1993). Here, we restrict ourselves to hydrodynamic models of the motion of a contact line. In this framework, for a completely wetting liquid, the viscous drag per unit length of a triple line moving perpendicular to itself also scales as $\gamma Ca^{2/3}$ (de Gennes *et al.* 2004). Following de Gennes (1985) and Eggers & Stone (2004), the drag per unit length exerted on a contact line advancing in the direction normal to itself may be more precisely written as

$$f_a \simeq 1.44 \gamma Ca^{2/3} \ell^{2/3} \tag{2.10}$$

For a contact line advancing on a dry substrate, ℓ is usually expressed as a logarithmic factor that depends on the detail of the physical and geometrical aspects of the model. It is often expressed in the following form:

$$\ell = \ln\left(\frac{\ell_M}{\ell_m}\right) \tag{2.11}$$

where ℓ_M and ℓ_m are the macroscopic and microscopic cutoff sizes. In the case of a drop sliding on a solid substrate, ℓ_M is commonly understood as a static scale such as the size of the drop (de Gennes 1985). In our experiments, we choose the thickness of the cell as the macroscopic cutoff and set $\ell_M \simeq h$. Typically, $\ell_M = 1$ mm. The microscopic cutoff size ℓ_m is usually taken as a molecular size or is related to the presence of a precursor film ahead of the wetting front. Here, we choose $\ell_m = 1$ Å. In making this choice, we set the value of $\ell = \ln(\ell_M/\ell_m) \simeq \ln 10^7 \simeq 16$. To compute the force acting on the front half of the drop, where the contact lines advance, one has to note that the local velocity of the advancing lines is not the drop velocity V but its projection on the direction normal to the line. For receding lines, the force per unit length f_a also needs to be projected on the direction of motion of the drop and integrated along the drop boundary to give the total force on the advancing lines at the front of the drop,

$$F_a \simeq 4.9 \gamma R C a^{2/3} \ell^{2/3} \tag{2.12}$$

The predicted total viscous force from the drop boundaries is then

$$F_{\eta_{line}} = F_r + F_a \simeq 43.9 \gamma R C a^{2/3} \tag{2.13}$$

Comparison with equation 2.5 gives a predicted value of $\beta \simeq 3.5$.

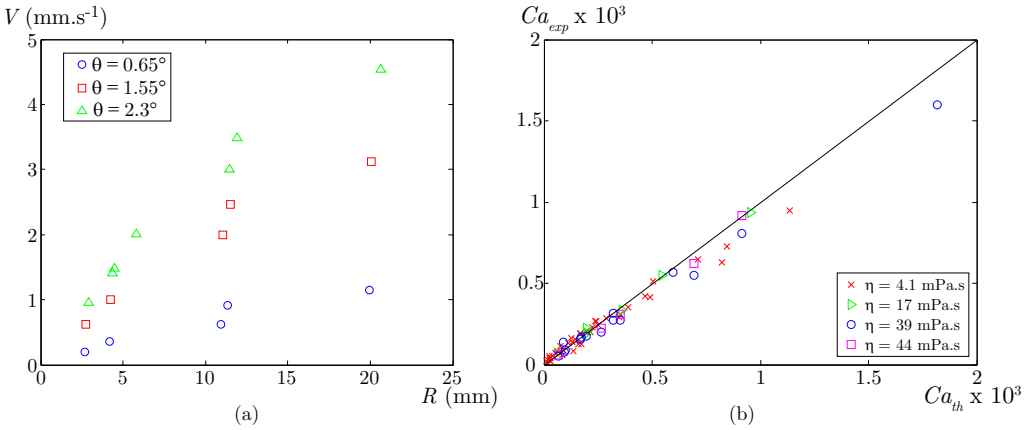

FIGURE 3. (a) Sliding velocity V of drops of silicone oil of viscosity $\eta = 4.1$ mPa.s bridging the two parallel walls of a Hele-Shaw cell of thickness $h = 1100$ μm. V increases with the radius R of the drops, and with the apparent gravity, *i.e.* with the tilt angle θ of the cell. (b) Measured sliding velocity of drops in a Hele-Shaw cell, expressed in terms of the capillary number $Ca_{exp} = \eta V/\gamma$ as a function of the prediction Ca_{th} of equation 2.15 with $\beta = 3.6$. The viscosity η of the oils ranges from 4.1 to 44 mPa.s, the drop volume Ω is between 14 and 1500 μL, the cell thickness h is between 150 and 1100 μm and the tilt angle θ ranges from 1.4° to 7°. Equation 2.15 is a good prediction of the measured capillary number Ca_{exp}.

2.2.3. *Equation of motion*

The equation of motion of the drop then simply relies on the balance of the apparent weight W with the viscous forces:

$$W = F_{\eta_{bulk}} + F_{\eta_{line}} \tag{2.14}$$

or

$$\pi R^2 h \rho g \sin\theta = 12\frac{\pi R^2}{h}\gamma Ca + 4\pi R\beta\gamma Ca^{2/3} \tag{2.15}$$

The mathematical structure of this equation is close to that describing the fall of liquid slugs under their own weight in capillary tubes (Bico & Quéré 2001). Both contributions to viscous friction are of the same order when $Ca^{1/3} \sim h/R$ or $Ca \sim (h/R)^3$. If $Ca > (h/R)^3$ dissipation from the bulk dominates. Otherwise, the contact lines contribute most.

2.3. *Discussion of experimental results*

As shown in figure 3a, drops with large radii slide faster than small ones. As the gap h of the cell is reduced, the viscous dissipation increases and the drops move more slowly. As expected, larger tilt angles θ correspond to a higher effective gravity field and lead to larger velocities.

In figure 3b we plot the measured capillary number Ca_{exp} of sliding drops as a function of the theoretical prediction Ca_{th} of equation 2.15. We adjust the value of the parameter β to obtain the best agreement between the experimental results and the model prediction, *i. e.* to minimize the mean-square deviation between Ca_{exp} and Ca_{th}. Here the optimal value $\beta \simeq 3.6$ enables all our data to be described by equation 2.15. This result is very close to the predicted value of $\beta = 3.5$.

Our model assumes that the drops are circular. Experimentally, we observe that the drops indeed remain discoids at moderate sliding velocities. As V increases, the drops tend to elongate perpendicular to the sliding direction. Here, we make sure that the length to width ratio of the drops remains between 0.9 and 1. The pressure that maintains the

coin shape of a drop is of order $P \sim \gamma/R$, which is the part of the Laplace pressure linked to deformations in the plane of the Hele-Shaw cell. The resulting pressure force is of order $PRh \sim \gamma h$. The viscous forces associated to the flow of liquid in the drop scale as $\gamma CaR^2/h$ if bulk dissipation dominates the contact line contributions. One expects the drops to maintain a circular shape as long as the capillary force overcomes the viscous friction. This can be written dimensionally as $\gamma h > \gamma CaR^2/h$ or

$$Ca < \left(\frac{h}{R}\right)^2 \tag{2.16}$$

Circular drops can thus be observed in the bulk dissipation regime ($Ca > (h/R)^3$) under the following conditions:

$$\left(\frac{h}{R}\right)^3 < Ca < \left(\frac{h}{R}\right)^2 \tag{2.17}$$

In our experiments, h is a fraction of a millimetre and $R \sim 10$ mm, so that this criterion predicts strong drop deformations for $Ca \gtrsim 5\times10^{-3}$, close to the highest value of Ca_{exp} in our experiments, as shown in figure 3b. In the regime dominated by contact line friction, the viscous force scales as $\gamma RCa^{2/3}$. The criterion 2.16 thus becomes

$$Ca < \left(\frac{h}{R}\right)^{3/2} \tag{2.18}$$

As shown above, line dissipation dominates when $Ca < (h/R)^3$. Since $h/R \ll 1$, we expect the criterion 2.18 to always be verified: in this regime, the drops are not deformed by the flow. In the following, we assume that we stay in regimes where the drops have a circular boundary.

The validity of equation 2.15 is also limited to pure Newtonian fluids. It has, for instance, been shown (Maruvada & Park 1996; Bush 1997; Verneuil *et al.* 2009; Selva *et al.* 2011) that surfactants change the structure of the flow around a bubble drifting in a thin gap. Marangoni effects are likely to affect the motion of drops as well. More generally, any complexity in the rheology of the fluid may induce deviations from the model presented here. Again, we exclude these effects in the following.

3. Drops in wedges

3.1. *Experiments*

We now describe the spontaneous motion of a drop of silicone oil confined between two quasi-horizontal flat plates forming a wedge of angle α (Fig. 4a). The wedge is formed by two 10 cm wide, 25 cm long and 3 mm thick glass plates facing each other and separated along one edge by glass spacers of millimetric thickness. The wedge angle α is of order 1° and is known to within less than 0.1°. The plates are initially dry. A drop of oil bridging the plates is inserted with a syringe needle in the thickest part of the cell. We define the position x of a drop as the distance between the centre of the liquid bridge and the apex of the wedge. The oil viscosity η, measured with a capillary viscometer, ranges from 4.1 to 44 mPa.s. The oil surface tension γ depends very little on the liquids we used and ranges from 19.7 to 20.7 mN.m^{-1}.

As noticed by Hauksbee (1710), such drops migrate towards the most confined region with an accelerated motion. Figure 4b shows successive positions of a 20 μL drop of $\eta = 4.1$ mPa.s silicone oil migrating towards the apex of a wedge. In figure 5a we plot the positions of drops of various volumes and viscosities as a function of the time before

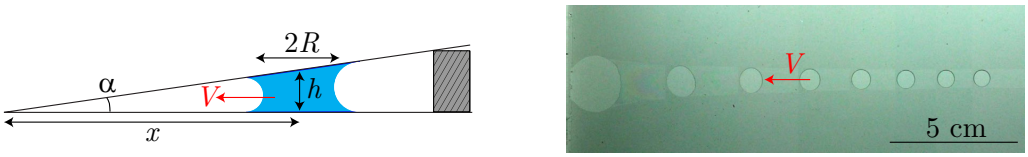

(a) (b)

FIGURE 4. (a) A drop of wetting fluid confined between two plates forming a wedge migrates toward the most confined region. (b) Superimposed images of a 20 μL drop of 5 cSt silicone oil confined in a wedge formed by two glass plates (top view). The drop moves toward the apex of the wedge located along the left boundary of the picture. The pictures were taken 0, 20, 40, 60, 80, 100, 120 and 140 s before the drop reached the tip.

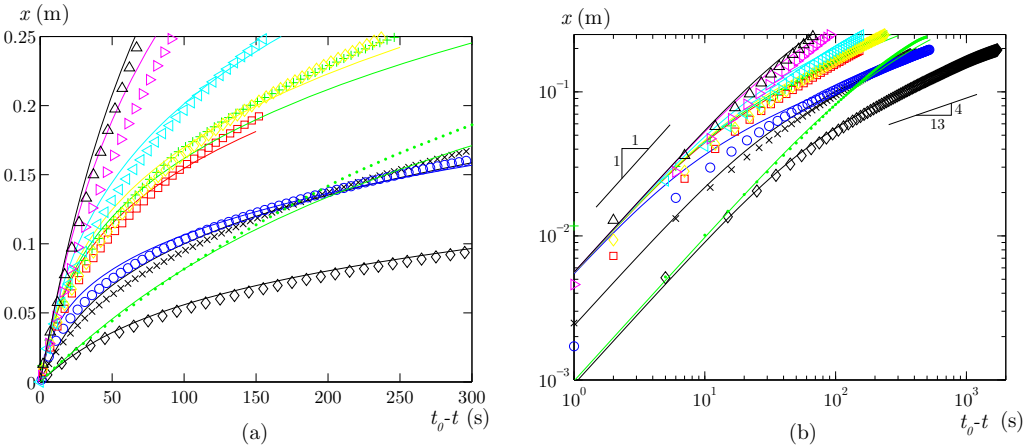

FIGURE 5. (a) Position of drops of silicone oils in a wedge as a function of the time $t_0 - t$ before they reach the apex. We show the trajectories of oil drop of viscosity $\eta = 4.1$ mPa.s and of volume 4.8 ($\circ$), 28 ($\square$), 35 ($+$), 45 ($\diamond$), 110 ($\triangleleft$), 750 ($\triangleright$), 1730 ($\triangle$) μL in a wedge with angle $\alpha = 0.40^\circ$. We plot one trajectory with a smaller angle: $\alpha = 0.071^\circ$, volume 4.5 μL ($\cdot$). We also show trajectories for drops of more viscous oils in a wedge with angle $\alpha = 0.68^\circ$. For those, the viscosities and drop volumes are 17.1 mPa.s/68 μL ($\times$) and 44 mPa.s/38 μL ($\lozenge$). Larger drops move faster. The symbols are experimental data. The full lines are plots of the solution of equation 3.6 with $\beta = 3.2$. (b) Same data plotted in logarithmic scale. Close to the tip, all drops have a constant velocity set by the fluid properties and wedge angle only. Far away from the edge, line dissipation dominates, and $x(t) \sim (t_0 - t)^{4/13}$, as predicted by equation 3.10. The cross-over between both regimes occurs closer to the apex for small drops.

they reach the end of the wedge. For a given viscosity, larger drops are observed to move faster than small ones. Moreover, by plotting the same data in logarithmic scale (figure 5b), one notices that close to the tip, the drop velocity is constant and does not depend on the drop size. Further away from the apex, the velocity is not constant and increases with the volume of the drop.

3.2. *Model*

Here, drops move under the influence of the confinement gradient. Close to the apex, the thickness of a drop decreases, leading to an increase of its radius due to volume conservation. Consequently, as it approaches the tip of a wedge, a drop wets a larger surface area Σ, which is energetically favourable for a totally wetting liquid such as silicone oil. For a totally wetting liquid, the capillary energy per unit area gained in advancing on a dry solid is the surface tension γ of the liquid. Contributions from the solid/liquid and solid/air interfacial tensions are actually dissipated in the formation

of a prewetting film ahead of the spreading contact line, as explained by de Gennes (1985). They thus drop out of the macroscopic energy balance. The capillary energy gain associated with a change $\mathrm{d}\Sigma$ of the contact area of the drop is thus $\mathrm{d}E_\gamma = \gamma \mathrm{d}\Sigma$. The force driving the drop towards the tip of the wedge is then

$$F_\gamma = -\frac{\mathrm{d}E_\gamma}{\mathrm{d}x} = -\gamma \frac{\mathrm{d}\Sigma}{\mathrm{d}x} \tag{3.1}$$

For a drop of volume Ω located at a distance x from the wedge, $\Sigma = 2\Omega/h(x)$ where $h(x) = \alpha x$ is the gap thickness at position x. Thus, the capillary force acting on the drop is

$$F_\gamma = -2\gamma \frac{\mathrm{d}}{\mathrm{d}x}\left(\frac{\Omega}{\alpha x}\right) \tag{3.2}$$

or

$$F_\gamma = 2\gamma \frac{\Omega}{\alpha x^2} \tag{3.3}$$

As developed above in section 2, the viscous forces resisting motion can be separated into two contributions $F_{\eta_{bulk}}$ and $F_{\eta_{line}}$, from the bulk and the contact lines respectively. Using volume conservation $\Omega = \pi R^2 h = \pi R^2 \alpha x$, one can rewrite these forces as a function of the drop position x,

$$F_{\eta_{bulk}} = 12 \frac{\Omega}{\alpha^2 x^2} \gamma Ca \tag{3.4}$$

$$F_{\eta_{line}} = 4\pi\beta\gamma \left(\frac{\Omega}{\pi\alpha x}\right)^{1/2} Ca^{2/3} \tag{3.5}$$

The balance of capillary and viscous forces thus yields the following equation for the motion of a drop:

$$\frac{\Omega}{\alpha x^2} = 6\frac{\Omega}{\alpha^2 x^2} Ca + 2\pi\beta \left(\frac{\Omega}{\pi\alpha x}\right)^{1/2} Ca^{2/3} \tag{3.6}$$

Equation 3.6 exhibits two asymptotic regimes. As the drop approaches the apex ($x \to 0$), bulk dissipation dominates, so that the capillary number is constant

$$Ca = \frac{\alpha}{6} \tag{3.7}$$

The predicted capillary number is simply proportional to α and is independent of the drop size and fluid properties. By noting that $V = -\dot{x}$ and integrating equation 3.7 gives the distance x from the drop to the edge can be obtained as a function of time:

$$x(t) = \frac{\alpha\gamma}{6\eta}(t_0 - t) \tag{3.8}$$

where t_0 is the time at which the drop reaches the apex.

At early stages of motion, the drop is far from the tip, and contact line dissipation dominates. In this limit ($x \to \infty$), equation 3.6 is rewritten as

$$Ca = \frac{1}{2\sqrt{2}\beta^{3/2}} \left(\frac{\Omega}{\alpha\pi x^3}\right)^{3/4} \tag{3.9}$$

In this regime, the migration velocity increases as the drop approaches the apex of the wedge, as noted by Hauksbee (1710). It also depends on the drop volume: large drops

migrate faster than small ones. Integration of equation 3.9 yields

$$x(t) = \left(\frac{13\gamma}{8\sqrt{2}\eta\beta^{3/2}} \left(\frac{\Omega}{\alpha\pi} \right)^{3/4} (t_0 - t) \right)^{4/13} \tag{3.10}$$

The crossover between the two asymptotic regimes occurs when both viscous forces have the same order of magnitude, $F_{\eta_{bulk}} \sim F_{\eta_{line}}$. This typically occurs when equations 3.7 and 3.9 give the same prediction for Ca. The position x^* of the transition between the two dissipation regimes is thus

$$x^* = a \frac{\Omega^{1/3}}{\beta^{2/3}\alpha^{7/9}} \tag{3.11}$$

where $a = 3^{4/9}/(2^{2/9}\pi^{1/3}) \simeq 0.954$. x^* is independent of the physical parameters of the liquid. Using equation 3.8, one finds that the drop reaches position x^* at a time $t_0 - t = t^*$ such that

$$t^* = b \frac{\eta}{\gamma} \frac{\Omega^{1/3}}{\alpha^{16/9}} \tag{3.12}$$

with $b = 3^{13/9}2^{7/9}/\pi^{1/3} \simeq 5.72$. We now define $X = x/x^*$ and $T = (t_0 - t)/t^*$. Using these scaled variables, the equation of motion 3.6 may be written in non-dimensional form as

$$1 = \frac{\mathrm{d}X}{\mathrm{d}T} + X^{3/2} \left(\frac{\mathrm{d}X}{\mathrm{d}T} \right)^{2/3} \tag{3.13}$$

The asymptotic regimes now read as

$$\frac{\mathrm{d}X}{\mathrm{d}T} = 1, \;\; X = T \tag{3.14}$$

for $X,\ T \ll 1$ and

$$\frac{\mathrm{d}X}{\mathrm{d}T} = \frac{1}{X^{9/4}}, \;\; X = \left(\frac{13}{4} T \right)^{4/13} \tag{3.15}$$

for $X,\ T \gg 1$.

3.3. *Discussion of experimental results*

We now compare the experimental measurements with the analytical results. The accelerated motion of drops towards the tip of the wedge, observed in figure 5, is predicted when dissipation in the boundaries dominates, far from the apex. In this regime, theory predicts that $x(t)$ should scale as $(t_0 - t)^{4/13}$ where t_0 is the time at which the drop reaches the point of the wedge. The smallest drops in widest wedges indeed start their trajectory following this scaling. In more confined regions, bulk dissipation dominates, and the asymptotic regime described by equation 3.7 predicts that drops should approach the tip of the wedge at constant velocity, which is also the trend observed in figure 5b. This regime is best observed for drops in the most acute wedges. Fitting of the entire trajectories of drops constitutes a stronger test of the model. In figure 5, we plot the positions of silicone oil drops as a function of time for different volumes, viscosities and wedge angles. The numerical solutions of equation 3.6 describe all the experimental trajectories very well with a single value of the prefactor for contact line friction, $\beta = 3.2 \pm 0.2$, within 10 % of the prediction and measurements from gravity driven drift described in section 2.

Finally, we use the dimensionless variables defined in section 3.2. In figure 6a, we plot experimental trajectories in the reduced form $X(T)$, using the value $\beta = 3.2$. Ω

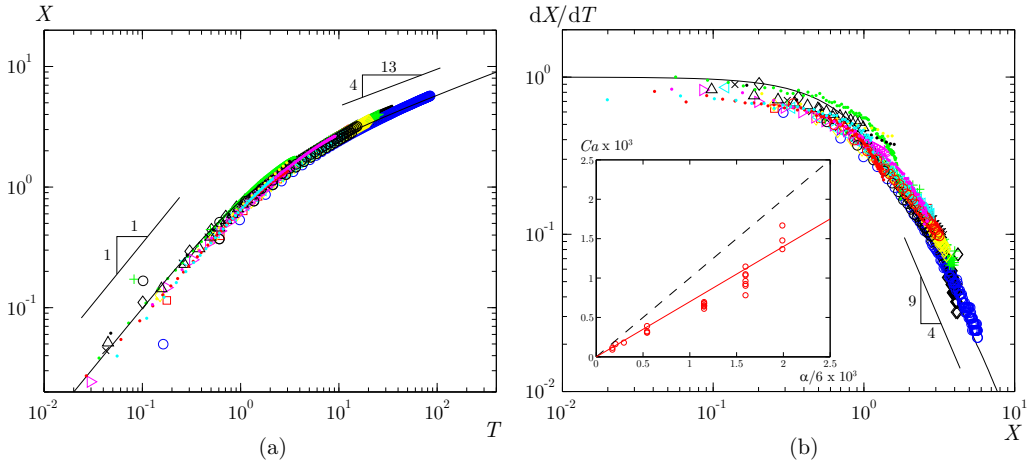

FIGURE 6. (a) Rescaled trajectories $X(T)$ of drops for different wedge angles ($0.07° < \alpha < 0.7°$), viscosities ($4.1 < \eta < 44$ mPa.s) and volumes ($4.5 < \Omega < 1750$ μL). The full line is the solution of equation 3.13 with $X(T = 0) = 0$. All the data collapse on this theoretical prediction. (b Main) Velocity of drops as a function of position in rescaled coordinates: $\mathrm{d}X/\mathrm{d}T$ vs X. All the data collapse on the same curve, and follow the prediction of equation 3.13 plotted as a continuous line. (b Inset) Measured capillary number of drops approaching the tip of a wedge as a function of the asymptotic prediction $\alpha/6$. The viscosity ranges from 4.1 to 44 mPa.s, and the volume of drops ranges from 4.5 to 1700 μL. The equation of the dashed line is $Ca = \alpha/6$, and the data is best fit by the line of equation $Ca \simeq 0.70\alpha/6$ (full line).

varies by a factor of more than 300, while α and η each span about one decade. We observe that all the data collapse to a single master curve which is the solution of the dimensionless equation of motion 3.13 with the initial condition $X(T = 0) = 0$. The line dissipation regime should be observed using very long plates compared with the transition position, $L \gg x^*$. Conversely, the pure bulk dissipation regime may be observed under the condition $x \ll x^*$, requiring $R \ll x^*$ at all times. While it is practically difficult to explore both dissipation regimes and estimate the crossover position x^* with one single drop, by plotting the rescaled data for many experiments the existence of the asymptotic limits predicted by equations 3.14 and 3.15 is clearly shown. The crossover between the two regimes is observed at $X = 1$, $T = 1$.

In figure 6b, we plot the rescaled velocities $\mathrm{d}X/\mathrm{d}T$ of drops as a function of their position X. Again, all the data collapse to the prediction of equation 3.13. The predicted asymptotic regimes (equations 3.14 and 3.15) are also observed here. Far away from the tip of the wedge ($X \gg 1$), the velocity decreases as $X^{-9/4}$. Close to the apex ($X \ll 1$), $\mathrm{d}X/\mathrm{d}T$ tends to saturate to a constant value. We extract the velocities of migrating drops just before they reach the wedge tip and plot the corresponding capillary numbers Ca as a function of the predicted value $\alpha/6$ in the inset to figure 6b. While Ω varies by a factor of more than 300 and η by about one decade, the measured capillary number varies only by about 30 % of its mean value for a given angle and thus appears to depend very weakly on Ω and η, in agreement with the prediction. The data are best described by a linear fit of the equation $Ca \simeq 0.70\alpha/6$, meaning that the drops are slightly slower than expected. The constant velocity regime should be observed in the region $x \ll x^*$. For the model to be valid, the variations of h over the drop size R should remain small, requiring $R \ll x$. The constant velocity regime should thus be observed under the following conditions: $R \ll x \ll x^*$. As R increases strongly close to the tip of the wedge, R/x^* is often not small enough to ensure $x \ll x^*$, so that drops hit the apex before reaching the smallest

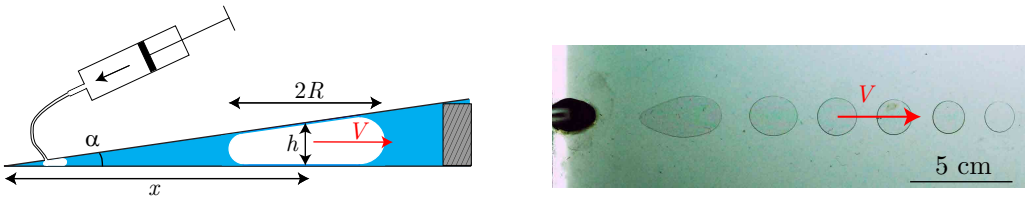

(a) (b)

FIGURE 7. (a) Using a syringe, an air bubble is injected in a wedge filled with wetting oil. Under the gradient of confinement, the bubble escapes the confined region to recover a more spherical shape, thus lowering the air/oil interface area. (b) Superimposed images of a 13 μL air bubble in 5 cSt silicone oil confined in a wedge formed by two glass plates (top view). The bubble moves away from the apex of the wedge located along the left boundary of the picture. The black line represents 5 cm, and the pictures were taken 3, 9, 15, 21, 27 and 33 s after the injection of the bubble into the wedge. Close to the injection point (dark spot on the left of the picture), the bubble is elongated along the motion direction. Further away for the wedge apex, it recovers a circular shape.

values of x. For many experiments, the bulk dissipation regime is not fully reached, so that the drop velocity remains slightly below the asymptotic value. Moreover, as a drop reaches the most confined regions ($R \gtrsim x$), its thickness is not homogeneous any longer. One then expects viscous dissipation to localize in the thinnest part of the drop, close to the apex of the wedge. This may explain the elongation of drops perpendicular to their motion direction observed in figure 4b. For a given migration velocity, this also means that dissipation occurs in a part of the drop thinner than its average thickness $h(x)$. One thus expects viscous effects to be stronger than they would be for a drop with homogeneous thickness. This effect would also tend to make the drops slower than predicted by our model. One last possible explanation for the drops being slower than expected lies in the deformability of the cell walls. In strongly confined regions, the Laplace pressure inside the drop is highly negative and tends to close the gap even more. Such flattening of the cell leads to a weaker driving force and stronger viscous dissipation, thus reducing the migration velocity.

4. Bubbles in wedges

4.1. *Experiments*

We now reverse the wetting condition and investigate the motion of a volume of non-wetting fluid in a wedge. The geometry of the experiment is the same as in the previous section. However, the gap between the plates is now filled with silicone oil. Using a syringe, we inject an air bubble through a millimetric hole pierced in the upper plate at approximately 1 cm from the apex of the wedge, as described in figure 7a. The volume Ω of the bubble ranges from 0.15 to 140 μL, the oil viscosity η is between 4.1 and 44 mPa.s, and its surface tension γ is close to 20 mN.m^{-1}. The wedge angle is still of order 1°. We now observe that the bubble tends to escape confinement with a decreasing velocity. For an oil of viscosity $\eta = 4.1$ mPa.s, the migration velocity is typically 1 mm.s^{-1}. As they depart from the wedge, the largest bubbles tend to be elongated in the direction of motion, as seen in figure 7b. They recover a discoidal shape further away from the injection hole.

4.2. *Model*

Since silicone oil is a totally wetting fluid for glass, the bubble is separated from the wall by a thin liquid film. In this case, air behaves as totally non-wetting and the bubble tends to escape from the apex of the wedge, so as to recover a spherical shape, minimizing the area of the liquid/air interface. As above, the driving force is linked to the confinement gradient. In the limit of circular flat confined air puddles, $h(x) \ll R$, the air/oil surface area is $\Sigma = 2\pi R^2 = 2\Omega/h(x)$, as was the contact area of drops on glass in the previous section. The force driving the bubble away from the apex of the wedge thus has the same expression as before, but it is now directed away from the tip, $F_\gamma = 2\gamma\Omega/\alpha x^2$.

We now discuss the viscous drag for an air bubble moving in a fluid confined between parallel walls. Here, the dissipation is localized in the liquid around the bubble. As for drops, we distinguish two separate regions: the bulk of the fluid, and the vicinity of boundaries.

The bulk contribution of viscous drag on a bubble rising in an inclined Hele-Shaw cell has been derived in the past by Siekmann *et al.* (1974),Eck & Siekmann (1978), citeMaxworthy1986 and Bush (1997). These authors show that the drag contribution for the fluid bulk has the same expression as the bulk contribution for drops,

$$F_{\eta_{bulk}} = 12\frac{\pi R^2}{h}\gamma Ca \tag{4.1}$$

This theoretical result is supported by experimental measurements of the drifting velocity of bubbles in Hele-Shaw devices (Bush 1997; Eri & Okumura 2011; Selva *et al.* 2011).

As in the previous section on drops, viscous dissipation in the vicinity of interfaces gives an additional contribution to the drag. Cantat (2013) recently reviewed the peculiar dissipation mechanisms associated with meniscus motion in this situation. In the case of stress-free liquid-air interfaces, which corresponds to the present surfactant-free silicone oil, the force per unit length of a receding or advancing meniscus is shown to scale as $\gamma c a^{2/3}$. We will here assume as in the previous section on drops that close to the bubble boundaries, the flow is directed normal to the boundaries, as observed by Rio *et al.* (2005) in a closely related situation. Meniscii along the front half of the bubble are receding and leaving a fluid film behind them. The drag contribution from the front of the bubble is then calculated exactly as for the rear of a drop in the previous configuration, and has the same expression,

$$F_r \simeq 12.9\gamma R C a^{2/3} \tag{4.2}$$

At the rear of the bubble, liquid advances on the film deposited by the front meniscii. Cantat (2013) provides the force per unit length in this particular situation of a meniscus advancing on a film deposited by a receding line moving at the same velocity,

$$f_a \simeq 1.1\gamma c a^{2/3} \tag{4.3}$$

Again, we project this force along the main motion direction and integrate it along the rear boundaries of the bubble to get the force associated with advancing interfaces,

$$F_a \simeq 3.7\gamma R C a^{2/3} \tag{4.4}$$

The total drag contribution from boundaries is thus written as

$$F_{\eta_{line}} = F_r + F_a \simeq 16.6\gamma R C a^{2/3} \tag{4.5}$$

or

$$F_{\eta_{line}} \simeq 4\pi\chi\gamma R C a^{2/3} \tag{4.6}$$

where $\chi \simeq 1.32$. The drag from boundaries thus scales similarly for drops and bubbles:

only the numerical prefactor differs due to the details of the contact lines. We notice that $\chi < \beta$: the rear meniscus of a bubble advances on the liquid film deposited by the front of the bubble while the front line of a drop progresses on dry solid and experiences stronger viscous friction.

We can now write the equation of motion of the bubble by balancing the driving capillary force with both drag contributions. The only difference from the drop analysis is the numerical coefficient χ that replaces β in the viscous resistance associated to boundaries. The migration of a bubble is thus governed by the same equation as that describing the motion of a drop in a dry wedge 3.6 in which β is changed to χ,

$$\frac{\Omega}{\alpha x^2} = 6\frac{\Omega}{\alpha^2 x^2}Ca + 2\pi\chi\left(\frac{\Omega}{\pi\alpha x}\right)^{1/2} Ca^{2/3} \tag{4.7}$$

The only differences here are the numerical factor in the contact line viscous force and the fact that $V = +\dot{x}$. This equation is actually the limit of uniform surface tension γ of the result derived by Selva *et al.* (2011). Since the motion equations for drops and bubbles are essentially identical, one recovers the same laws as above for $x(t)$ by simply replacing β by χ and $t_0 - t$ by $t - t_0$. Here t_0 is the interpolated time at which the bubble departs from the apex of the wedge. Thus, at short times ($x \to 0$), the capillary number is constant,

$$Ca = \frac{\alpha}{6} \tag{4.8}$$

and the position of the bubble is

$$x(t) = \frac{\alpha\gamma}{6\eta}(t - t_0) \tag{4.9}$$

Far from the ridge ($x \to \infty$), the velocity depends on the volume of the bubble and it decreases as the bubble moves away from the tip. The capillary number is given by

$$Ca = \frac{1}{2\sqrt{2}\chi^{3/2}}\left(\frac{\Omega}{\alpha\pi x^3}\right)^{3/4} \tag{4.10}$$

and the bubble position is

$$x(t) = \left(\frac{13\gamma}{8\sqrt{2}\eta\chi^{3/2}}\left(\frac{\Omega}{\alpha\pi}\right)^{3/4}(t - t_0)\right)^{4/13} \tag{4.11}$$

Due to the similarity between the bubble and drop problems, equation 4.7 may be non-dimensionalized in the same way as for drops, by simply replacing β by χ and changing $t_0 - t$ into $t - t_0$. We thus define the position x_b^* at which both dissipation terms are of the same order by

$$x_b^* = a\frac{\Omega^{1/3}}{\chi^{2/3}\alpha^{7/9}} \tag{4.12}$$

The bubble reaches x_b^* at a time $t - t_0 = t_b^*$ such that

$$t_b^* = b\frac{\eta}{\gamma}\frac{\Omega^{1/3}}{\alpha^{16/9}} \tag{4.13}$$

Using the rescaled variables $X = x/x_b^*$ and $T = t/t_b^*$, the equation of motion for bubbles is equation 3.13, as for drops. In terms of X and T, the asymptotic regimes are thus unchanged.

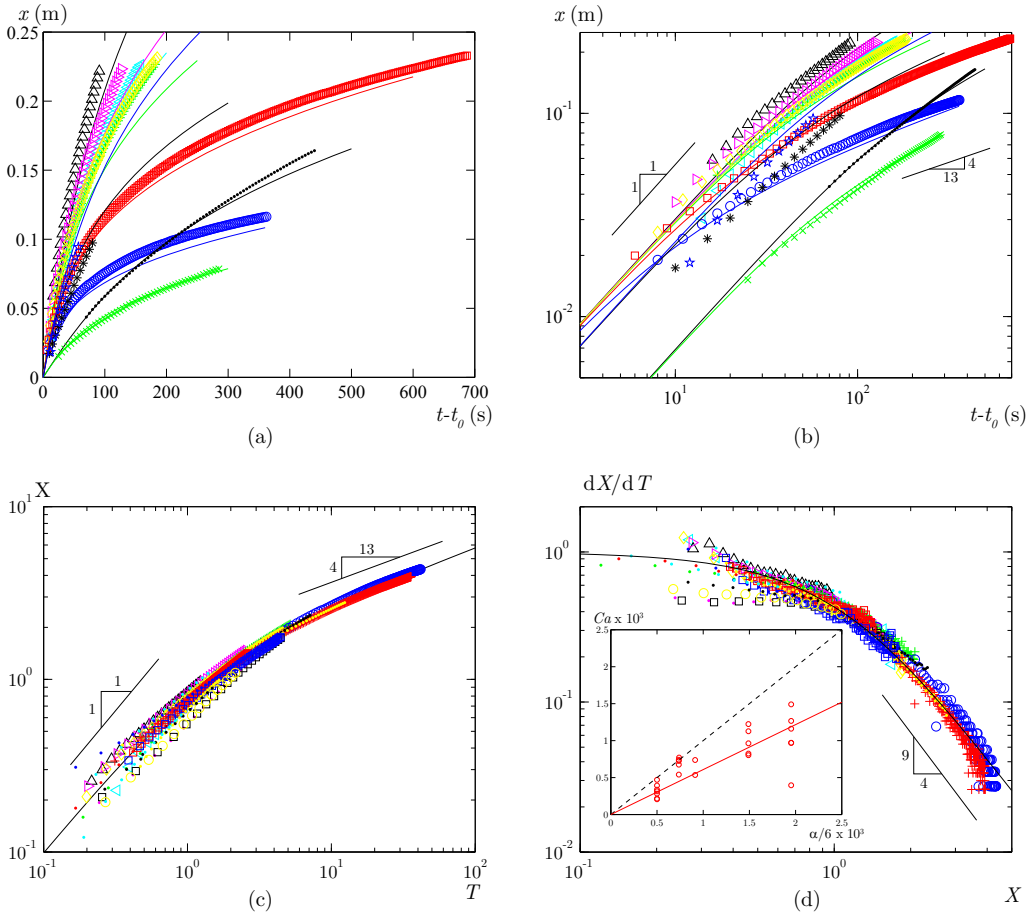

FIGURE 8. (a) Position of air bubbles in a wedge filled with silicone oil as a function of the time $t - t_0$ after they left the apex. We show the trajectories of bubbles of volume 0.15 ($\circ$), 1.3 ($\square$), 8 ($+$), 12 ($\Diamond$), 15 ($\triangleleft$), 22 ($\triangleright$) and 75 ($\triangle$) μL in oil of viscosity $\eta = 4.1$ mPa.s in a wedge of angle $\alpha = 0.25°$. Larger bubbles move faster. We plot trajectories with a smaller wedge angle: $\alpha = 0.17°$, volume $\Omega = 1.8$ ($\ast$) and 8.8 ($\star$) μL. We also show trajectories for bubbles in more viscous oil, $\eta = 44$ mPa.s, with volumes 2.8 ($\times$) and 49 ($\cdot$) μL and $\alpha = 0.51°$. The open symbols are experimental data, the full lines are the corresponding numerical solutions of equation 4.7 with $\chi = 1.3$. (b) The same data are plotted in logarithmic scale. Close to the tip of the wedge, bubbles start with a constant velocity that depends on geometry and fluid viscosity and surface tension. Far away from the apex, line dissipation dominates, and $x(t) \sim (t - t_0)^{4/13}$, as predicted by equation 4.11. The cross-over between both regimes occurs closer to the edge for small bubbles. (c) Rescaled trajectories $X(T)$ of bubbles for different wedge angles ($0.17° \leqslant \alpha \leqslant 0.51°$), fluid viscosities ($4.1 \leqslant \eta \leqslant 44$ mPa.s) and volumes ($0.15 \leqslant \Omega \leqslant 140$ μL). The full line is the solution of equation 3.13 with $X(T = 0) = 0$. All the data collapse on this theoretical prediction. (d Main) Velocity $\mathrm{d}X/\mathrm{d}T$ of air bubbles as a function of position X in rescaled coordinates. All the data collapse on the same curve, following the prediction of equation 3.13 plotted as a continuous line. At small values of X and T, some scatter is likely due to the deformations of bubbles and walls of the cell. (d Inset) Measured capillary number of bubbles escaping the tip of a wedge as a function of the asymptotic prediction $\alpha/6$. The viscosity range from 4.1 to 44 mPa.s, and the volume of drops range from 0.15 to 140 μL. The equation of the dashed line is $Ca = \alpha/6$, and the data is best fit by the line of equation $Ca \simeq 0.61\alpha/6$ (full line).

4.3. *Discussion of experimental results*

In figure 8a we plot trajectories of bubbles of different volumes in wedges of different angles filled with silicone oils of viscosity $\eta = 4.1$ and 44 mPa.s. As they escape confinement, the bubbles are observed to slow down, in agreement with the model. The scaling regimes predicted by equations 4.9 and 4.11 are indeed approached, as shown in figure 8b. Numerical solutions of equation 4.7 describe the experimental trajectories very well. As for drops, one single value of the prefactor for interfacial dissipation gives a good description of all experiments. Here, $\chi = 1.3 \pm 0.2$, in excellent agreement with the prediction of equation 4.5.

Figure 8c shows all the bubble trajectories in reduced coordinates $X(T)$, using the value $\chi = 1.3$. The bubble volume Ω ranges from 0.15 to 140 μL, α is between 0.17° and 0.51° and the oil viscosity η spans one decade. All the data collapse to the numerical solution of equation 3.13 with initial condition $X(T = 0) = 0$.

We also plot the rescaled velocity $\mathrm{d}X/\mathrm{d}T$ as a function of X in figure 8d. While the collapse is again fairly good, some deviations are observed. At long times (X, $T \gg 1$), the velocity of the smallest bubbles tends to be smaller than the prediction of our model. As they move away from the tip of the wedge, the bubbles recover a spherical shape. They are not confined any longer, and thus do not feel the driving gradient of the gap thickness. The motion then stops, except for a possible very slow drift under gravity due to the slight slope of the upper confining plate. At short times (X, $T \ll 1$), figure 8d shows significant scatter in the dimensionless bubble velocity. Typically, $\mathrm{d}X/\mathrm{d}T$ is within a factor of about 2 of the prediction of the model. As for drops, we expect our model to be valid under the assumptions $R \ll x \ll x_b^*$. The second condition is not fully satisfied in systems with a small value of x_b^*, while the first inequality breaks down very close to the tip of the wedge, resulting in deformation of the largest bubbles. In contrast to the drops, these stretch along the direction of motion, as shown by the image superposition in figure 7b. Such bubbles do not have the circular boundary assumed by the model. Finally, we note that the scatter observed in the velocities close to the ridge is stronger for bubbles than for drops. One possible reason is that the viscous flow is external to a bubble, so that the influence of the walls on the motion extends over a distance greater than the size of the bubble. As a consequence, the apex of the wedge may perturb the shape of bubbles at long distances. For drops, the viscous stresses are confined inside the perimeter and the influence of the tip of the wedge is reduced.

5. Power-law-shaped wedges

The plates forming the wedge do not need to be flat, and complex gap profiles are common, for instance close to fracture fronts in solids. Here, we restrict our study to the case of power-law-shaped wedges: $h(x) = Ax^\delta$, where $\delta > 0$. We consider the case of a drop of wetting viscous fluid in an otherwise empty wedge. The capillary driving force and both viscous forces can thus be rewritten using this new expression for the gap thickness. One obtains

$$F_\gamma = 2\frac{\gamma\delta\Omega}{Ax^{\delta+1}} \tag{5.1}$$

$$F_{\eta_{bulk}} = 12Ca\frac{\gamma\Omega}{A^2x^{2\delta}} \tag{5.2}$$

$$F_{\eta_{line}} = 4\pi\beta\gamma\left(\frac{\Omega}{\pi Ax^\delta}\right)^{1/2} Ca^{2/3} \tag{5.3}$$

As in previous sections, these expressions remain true as long as the gap variations are small on the scale of the size R of the drop, $R\mathrm{d}h/\mathrm{d}x \ll h(x)$ or $\delta R/x \ll 1$.

We then follow the reasoning developed in previous sections. Close to the tip of the wedge, bulk dissipation dominates so that $F_\gamma = F_{\eta_{bulk}}$. The equation of motion of the drop is thus of the form

$$\dot{x}x^{1-\delta} = -\frac{\gamma A\delta}{6\eta} \tag{5.4}$$

As for straight wedges, the dynamics are independent of the drop volume in this regime. Integration of equation 5.4 gives the position of the drop as a function of time. For $0 < \delta < 2$:

$$x(t) = \left(\frac{\gamma A\delta(2-\delta)}{6\eta}\right)^{\frac{1}{2-\delta}} (t_0 - t)^{\frac{1}{2-\delta}} \tag{5.5}$$

and the drop reaches the wedge tip at a finite time t_0. In particular, one recovers $x(t) \sim t_0 - t$ for $\delta = 1$. For $\delta = 2$, one obtains

$$x(t) = x_0 \exp\left(-\frac{\gamma A}{3\eta}t\right) \tag{5.6}$$

where x_0 is the initial position of the drop. For $\delta > 2$,

$$x(t) = \frac{x_0}{\left(1 + \frac{\gamma A\delta(\delta-2)x_0^{\delta-2}}{6\eta}t\right)^{\frac{1}{\delta-2}}} \tag{5.7}$$

In these cases, the confinement gradient close to the tip decreases strongly, which accounts for the slow dynamics predicted: the drop does not reach the apex in a finite time. In practice, however, we observe that drops tend to strongly deform in such wedges. Our analysis relies on the assumption that drops maintain a discoidal shape and may thus break down in this limit.

Far away from the apex, contact lines dominate the dissipation processes. The equation of motion is thus $F_\gamma = F_{\eta_{line}}$ and can be written as

$$\dot{x}x^{\frac{3}{2}+\frac{3\delta}{4}} = -\frac{\gamma}{\eta}\left(\frac{\Omega\delta^2}{4\pi A\beta^2}\right)^{3/4} \tag{5.8}$$

As in straight wedges, large drops move faster than small ones. The position of the drop follows

$$x(t) \sim (t_0 - t)^{\frac{4}{10+3\delta}} \tag{5.9}$$

Again, on setting $\delta = 1$ we recover the dynamics derived above for a straight wedge, $x(t) \sim (t_0 - t)^{4/13}$.

6. Conclusion

We have shown experimentally that drops of wetting liquids confined in model porous systems are driven towards the most confined regions by capillary forces. These balance the viscous forces in the bulk of the drop and in contact lines, setting the dynamics of the motion. Two distinct asymptotic regimes are observed depending on the relative strength of the bulk and contact line viscous dissipation. The crossover between the two limits is used to derive a dimensionless equation of motion. All experimental data collapse to the numerical solution of this rescaled model. The problem of air bubbles migrating in a wedge immersed with oil is described by the same dimensionless theory. A simple analysis

yields predictions for different scaling regimes in wedges with more complex power-law shapes.

In the model system presented in this paper, the drop dynamics are strongly determined by the viscous dissipation at the contact line. We believe that similar experiments would be good candidates to test the physics of this singular region. Confined drops moving on liquid-coated plates may indeed enable control of the contact line singularity. From an applied point of view, manipulation of drops under confinement gradients is useful to the field of microfluidics (Dangla *et al.* 2013; Selva *et al.* 2011) and may be coupled with transverse flows to achieve sorting of drops or elastic objects such as living cells with different structures, sizes, surface tension or Young modulus.

Confinement is associated to strong capillary effects, as the Laplace pressure is inversely proportional to the characteristic size of liquid meniscii. High negative capillary pressures induced close to the tip of a fracture are sufficient to locally deform the environment, inducing the closure of wet fractures in materials as hard as silica glass (Pallares *et al.* 2011). Extension of our problem to the case of a wedge with elastic boundaries will provide an interesting model system to shed light on the dynamics of wet fracture closure.

Finally, drops in wedges also constitute a model situation for detergency or oil extraction. It would be interesting to investigate the physico-chemical mechanisms enabling one to extract the oil from the wedge using another liquid with a more favourable wetting condition.

It is a pleasure to thank Thomas Cambau for preliminary experiments, Camille Duprat and Marie-Caroline Jullien for helpful discussions, and Mathilde Reyssat, José Bico and Mark Weislogel for careful reading of the manuscript. This research has been funded by the Interuniversity Attraction Poles Programme (IAP 7/38 MicroMAST) initiated by the Belgian Science Policy Office.

REFERENCES

Bico, José & Quéré, David 2001 Falling Slugs. *Journal of colloid and interface science* **243**, 262–264.

Bonn, Daniel, Eggers, Jens, Indekeu, Joseph, Meunier, Jacques & Rolley, Etienne 2009 Wetting and spreading. *Reviews of Modern Physics* **81** (2), 739–805.

Bouasse, Henri 1924 *Capillarité, phénomènes superficiels*. Paris: Delagrave.

Boudaoud, Arezki 2007 Non-Newtonian thin films with normal stresses: dynamics and spreading. *The European physical journal. E, Soft matter* **22** (2), 107–109.

Brochard, Françoise 1989 Motion of Droplets on Solid Surfaces Induced by Chemical or Thermal Gradients. *Langmuir* **5** (3), 432–438.

Bush, John W. M. 1997 The anomalous wake accompanying bubbles rising in a thin gap: a mechanically forced Marangoni flow. *Journal of Fluid Mechanics* **352**, 283–303.

Cantat, Isabelle 2013 Liquid meniscus friction on a wet plate: Bubbles, lamellae, and foams. *Physics of Fluids* **25** (3), 031303.

Chaudhury, M. K. & Whitesides, G. M. 1992 How to make water run uphill. *Science* **256** (5063), 1539–1541.

Dangla, Rémi, Kayi, S Cagri & Baroud, Charles N 2013 Droplet microfluidics driven by gradients of confinement. *Proceedings of the National Academy of Sciences of the United States of America* **110** (3), 853–8.

Daniel, Susan, Sircar, Sanjoy, Gliem, Jill & Chaudhury, Manoj K 2004 Ratcheting motion of liquid drops on gradient surfaces. *Langmuir* **20** (10), 4085–4092.

Domingues dos Santos, Fabrice & Ondarçuhu, Thierry 1995 Free-Running Droplets. *Physical Review Letters* **75** (16), 2972–2975.

Eck, W. & Siekmann, J. 1978 On Bubble Motion in a Hele-Shaw Cell, a Possibility to Study Two-Phase Flows under Reduced Gravity. *Ingenieur-Archiv* **47**, 153–168.

Eggers, Jens & Stone, Howard A. 2004 Characteristic lengths at moving contact lines for a perfectly wetting fluid: the influence of speed on the dynamic contact angle. *Journal of Fluid Mechanics* **505**, 309–321.

Eri, Ayako & Okumura, Ko 2011 Viscous drag friction acting on a fluid drop confined in between two plates. *Soft Matter* **7** (12), 5648–5653.

de Gennes, Pierre-Gilles 1985 Wetting: statics and dynamics. *Reviews of Modern Physics* **57** (3), 827–863.

de Gennes, Pierre-Gilles, Brochard-Wyart, Françoise & Quéré, David 2004 *Capillarity and wetting phenomena: drops, bubbles, pearls and waves*. New York: Springer.

Genzer, Jan & Bhat, Rajendra R. 2008 Surface-Bound Soft Matter Gradients. *Langmuir* **24**, 2294–2317.

Gorodtsov, V. A. 1989 Spreading of a film of nonlinearly viscous liquid over a horizontal smooth solid surface. *Journal of Engineering Physics* **57** (2), 879–884.

Greenspan, H. P. 1978 On the motion of a small viscous droplet that wets a surface. *Journal of Fluid Mechanics* **84**, 125–143.

Hauksbee, Fr. 1710 An Account of an Experiment Touching the Direction of a Drop of Oil of Oranges, between Two Glass Planes, towards Any Side of Them That is Nearest Press'd Together. By Mr. Fr. Hauksbee, F. R. S. *Philosophical Transactions of the Royal Society of London* **27** (325-336), 395–396.

Huh, Chun & Scriven, L. E. 1971 Hydrodynamic Model of Steady Movement of a Solid / Liquid / Fluid Contact Line. *Journal of colloid and interface science* **35** (1), 85–101.

Jacqmin, David 2000 Contact-line dynamics of a diffuse fluid interface. *Journal of Fluid Mechanics* **402**, 57–88.

Landau, Lev & Levich, Veniamin G. 1942 Dragging of a liquid by a moving plate. *Acta Physicochimica USSR* **17**, 42.

Lo, Chun-min, Wang, Hong-bei, Dembo, Micah & Wang, Yu-li 2000 Cell Movement Is Guided by the Rigidity of the Substrate. *Biophysical Journal* **79** (1), 144–152.

Lorenceau, Elise & Quéré, David 2004 Drops on a conical wire. *Journal of Fluid Mechanics* **510**, 29–45.

Malvadkar, N. A., Hancock, M. J., Sekeroglu, K., Dressick, W. J. & Demirel, M. C. 2010 An engineered anisotropic nanofilm with unidirectional wetting properties. *Nature Materials* **9** (October), 1023–1028.

Maruvada, S R K & Park, C W 1996 Retarded motion of bubbles in Hele-Shaw cells. *Physics of Fluids* **8**, 3229–3233.

Metz, Tobias, Paust, Nils, Zengerle, Roland & Koltay, Peter 2009 Capillary driven movement of gas bubbles in tapered structures. *Microfluidics and Nanofluidics* **9** (2-3), 341–355.

Pallares, Gaël, Grimaldi, Antoine, George, Matthieu, Ponson, Laurent & Ciccotti, Matteo 2011 Quantitative Analysis of Crack Closure Driven by Laplace Pressure in Silica Glass. *Journal of the American Ceramic Society* **94** (8), 2613–2618.

Prakash, Manu, Quéré, David & Bush, John W M 2008 Surface tension transport of prey by feeding shorebirds: the capillary ratchet. *Science* **320** (5878), 931–934.

Renvoisé, P., Bush, J. W. M., Prakash, M. & Quéré, D. 2009 Drop propulsion in tapered tubes. *EPL (Europhysics Letters)* **86** (6), 64003.

Reyssat, Mathilde, Pardo, Fabrice & Quéré, David 2009 Drops onto gradients of texture. *EPL* **87**, 36003.

Rio, E, Daerr, A, Andreotti, B & Limat, L 2005 Boundary Conditions in the Vicinity of a Dynamic Contact Line : Experimental Investigation of Viscous Drops Sliding Down an Inclined Plane. *Physical Review Letters* **94** (January), 024503.

Selva, Bertrand, Cantat, Isabelle & Jullien, Marie-Caroline 2011 Temperature-induced migration of a bubble in a soft microcavity. *Physics of Fluids* **23** (5), 052002.

Seppecher, Pierre 1996 Moving contact lines in the Cahn-Hilliard theory. *International Journal of Engineering Science* **34** (9), 977–992.

Siekmann, J., Eck, W. & Johann, W. 1974 Experimentelle Untersuchungen ûber das Verhalten von Gasblasen in einem Null-g-Simulator. *Zeitschrift für Flugwissenschaften* **22** (3), 83–92.

Style, Robert W, Che, Yonglu, Park, Su Ji, Weon, Byung Mook, Je, Jung Ho, Hy-

land, Callen, German, Guy K, Rooks, Michael, Wilen, Larry A, Wettlaufer, J S & Dufresne, Eric R 2013 Patterning droplets with durotaxis. *Proceedings of the National Academy of Sciences of the United States of America* **110**, 12541–12544.

Tanner, L. H. 1979 The spreading of silicone oil drops on horizontal surfaces. *Journal of Physics D: Applied Physics* **12**, 1473–1484.

Thompson, Peter A & Troian, Sandra M 1997 A general boundary condition for liquid flow at solid surfaces. *Nature* **389** (September), 360–362.

Verneuil, Emilie, Cordero, María Luisa, Gallaire, François & Baroud, Charles N. 2009 Laser-induced force on a microfluidic drop: origin and magnitude. *Langmuir* **25** (9), 5127–5134.

Wayner, Peter C. Jr. 1993 Spreading of a Liquid Film with a Finite Contact Angle by the Evaporation/Condensation Process. *Langmuir* **9** (14), 294–299.

Weislogel, Mark M 1997 Steady Spontaneous Capillary Flow in Partially Coated Tubes. *AIChE Journal* **43** (3), 645–654.

Weislogel, Mark M., Baker, J. Alex & Jenson, Ryan M. 2011 Quasi-steady capillarity-driven flows in slender containers with interior edges. *Journal of Fluid Mechanics* **685**, 271–305.

Weislogel, Mark M. & Lichter, S. 1996 A spreading drop in an interior corner: theory and experiment. *Microgravity Science and Technology* **9**, 175–184.

Zheng, Yongmei, Bai, Hao, Huang, Zhongbing, Tian, Xuelin, Nie, Fu-Qiang, Zhao, Yong, Zhai, Jin & Jiang, Lei 2010 Directional water collection on wetted spider silk. *Nature* **463** (7281), 640–643.